

The role of viscosity on drop impact forces

Vatsal Sanjay^{1†}, Bin Zhang^{2‡}, Cunjing Lv^{2¶}, and Detlef Lohse^{1,3||}

¹Physics of Fluids Group, Max Planck Center for Complex Fluid Dynamics, Department of Science and Technology, and J. M. Burgers Centre for Fluid Dynamics, University of Twente, P. O. Box 217, 7500 AE Enschede, The Netherlands

²Department of Engineering Mechanics, AML, Tsinghua University, Beijing 100084, China

³Max Planck Institute for Dynamics and Self-Organization, Am Fassberg 17, 37077 Göttingen, Germany

(Received xx; revised xx; accepted xx)

A liquid drop impacting a rigid substrate undergoes deformation and spreading due to normal reaction forces, which are counteracted by surface tension. On a non-wetting substrate, the drop subsequently retracts and takes off. Our recent work (Zhang et al., *Phys. Rev. Lett.*, vol. 129, 2022, 104501) revealed two peaks in the temporal evolution of the normal force $F(t)$ —one at impact and another at jump-off. The second peak coincides with a Worthington jet formation, which vanishes at high viscosities due to increased viscous dissipation affecting flow focusing. In this article, using experiments, direct numerical simulations, and scaling arguments, we characterize both the peak amplitude F_1 at impact and the one at take off (F_2) and elucidate their dependency on the control parameters: the Weber number We (dimensionless impact velocity) and the Ohnesorge number Oh (dimensionless viscosity). The first peak amplitude F_1 and the time t_1 to reach it depend on inertial timescales for low viscosity liquids, remaining nearly constant for viscosities up to 100 times that of water. For high viscosity liquids, we balance the rate of change in kinetic energy with viscous dissipation to obtain new scaling laws: $F_1/F_\rho \sim \sqrt{Oh}$ and $t_1/\tau_\rho \sim 1/\sqrt{Oh}$, where F_ρ and τ_ρ are the inertial force and time scales, respectively, which are consistent with our data. The time t_2 at which the amplitude F_2 appears is set by the inertia-capillary timescale τ_γ , independent of both the viscosity and the impact velocity of the drop. However, these properties dictate the magnitude of this amplitude.

Key words:

1. Introduction

Drop impacts have piqued the interest of scientists and artists alike for centuries, with the phenomenon being sketched by da Vinci (1508) in the early 16th and photographed by Worthington (1876a,b) in the late 19th century. It is, indeed, captivating to observe raindrops hitting a solid surface (Kim et al. 2020; Lohse & Villermaux 2020) or ocean spray affecting maritime structures (Berny et al. 2021; Villermaux et al. 2022). The phenomenology of drop impact is extremely rich, encompassing behaviors such as drop

† Email address for correspondence: vatsalsanjay@gmail.com

‡ Email address for correspondence: binzhang0710@mail.tsinghua.edu.cn

¶ Email address for correspondence: cunjinglv@mail.tsinghua.edu.cn

|| Email address for correspondence: d.lohse@utwente.nl

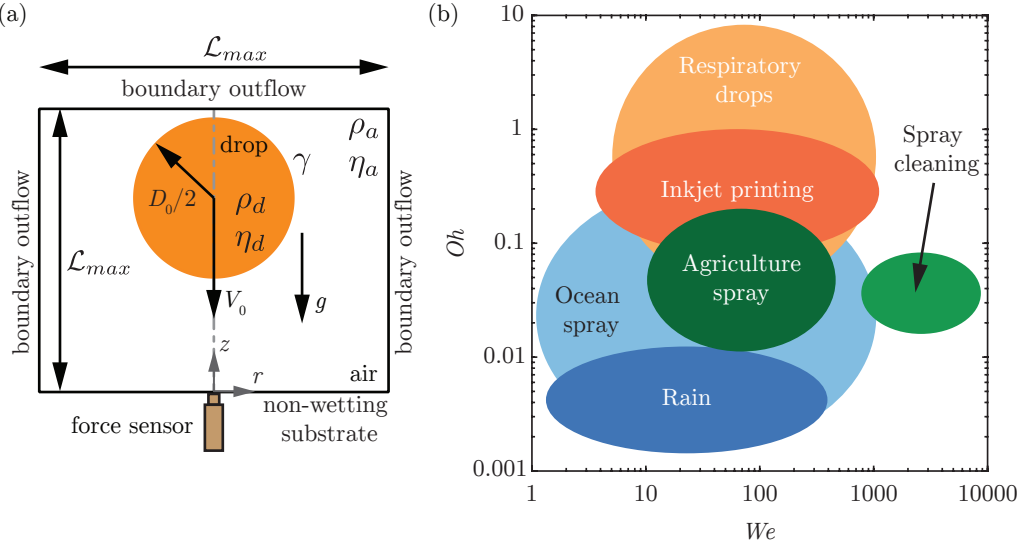


FIGURE 1. (a) Problem schematic with an axisymmetric computational domain used to study the impact of a drop with diameter D_0 and velocity V_0 on a non-wetting substrate. In the experiments, we use a quartz force sensor to measure the temporal variation of the impact force. The subscripts d and a denote the drop and air, respectively, to distinguish their material properties, which are the density ρ and the dynamic viscosity η . The drop-air surface tension coefficient is γ . The grey dashed-dotted line represents the axis of symmetry, $r = 0$. Boundary air outflow is applied at the top and side boundaries (tangential stresses, normal velocity gradient, and ambient pressure are set to zero). The domain boundaries are far enough from the drop not to influence its impact process ($L_{\max} \gg D_0$, $L_{\max} = 8R$ in the worst case). (b) The phase space with control parameters: the Weber number (We : dimensionless impact velocity) and the Ohnesorge number (Oh : dimensionless viscosity), exemplifying different applications.

deformation (Biance *et al.* 2006; Moláček & Bush 2012; Chevy *et al.* 2012), spreading (Laan *et al.* 2014; Wildeman *et al.* 2016), splashing Xu *et al.* (2005); Riboux & Gordillo (2014); Thoraval *et al.* (2021), fragmentation (Villermaux & Bossa 2011; Villermaux 2020), bouncing (Richard & Quéré 2000; Kolinski *et al.* 2014; Jha *et al.* 2020; Chubytsky *et al.* 2020; Sharma & Dixit 2021; Sanjay *et al.* 2023a), and wetting (de Gennes 1985; Fukai *et al.* 1995; Quéré 2008; Bonn *et al.* 2009). These behaviors are influenced by the interplay of inertial, capillary, and viscous forces, as well as additional factors like non-Newtonian properties (Bartolo *et al.* 2005, 2007; Smith & Bertola 2010; Gorin *et al.* 2022) of the liquid and even ambient air pressure (Xu *et al.* 2005), making the parameter space for this phenomenon both extensive and high-dimensional.

Naturally, even the process of a Newtonian liquid drop impacting a rigid substrate is governed by a plethora of control parameters, including but not limited to the drop's density ρ_d , diameter D_0 , velocity V_0 , dynamic viscosity η_d , surface tension γ , and acceleration due to gravity g (figure 1a). To navigate this rich landscape, we focus on two main dimensionless numbers that serve as control parameters (figure 1b): the Weber number We , which is the ratio of inertial to capillary forces and is given by

$$We = \frac{\rho_d V_0^2 D_0}{\gamma}, \quad (1.1)$$

and the Ohnesorge number Oh , which captures the interplay between viscous damping

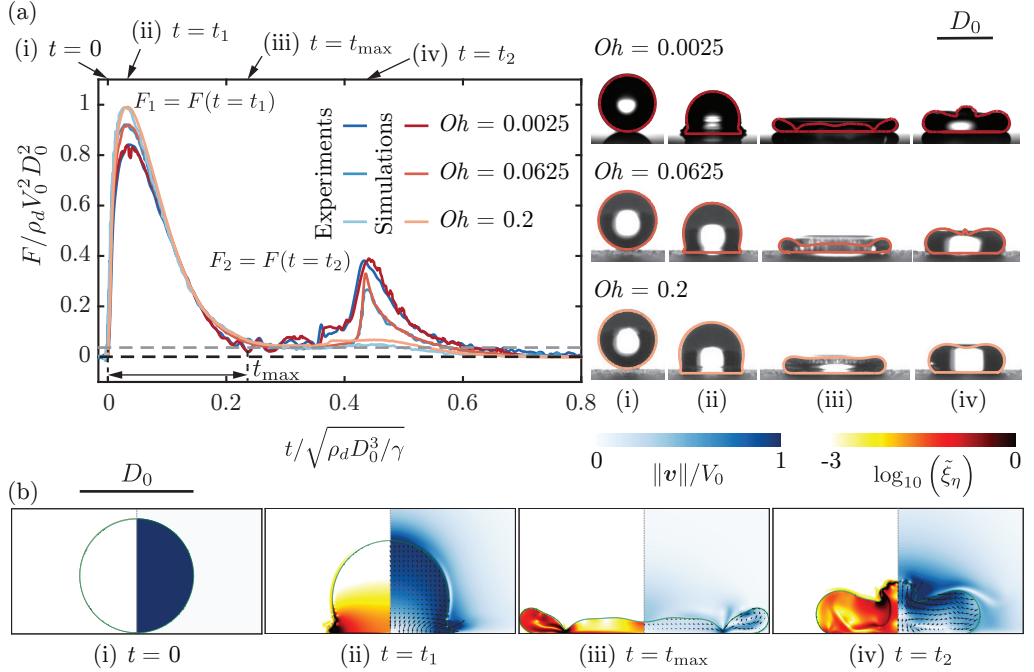


FIGURE 2. Comparison of the drop impact force $F(t)$ obtained from experiments and simulations for the three typical cases with impact velocity $V_0 = 1.2 \text{ m/s}, 0.97 \text{ m/s}, 0.96 \text{ m/s}$, diameter $D_0 = 2.05 \text{ mm}, 2.52 \text{ mm}, 2.54 \text{ mm}$, surface tension $\gamma = 72 \text{ mN/m}, 61 \text{ mN/m}, 61 \text{ mN/m}$ and viscosity $\eta_d = 1 \text{ mPa s}, 25.3 \text{ mPa s}, 80.2 \text{ mPa s}$. These parameter give $Oh = 0.0025, 0.0625, 0.2$ and $We = 40$. For the three cases, the two peak amplitudes, $F_1/\rho_d V_0^2 D_0^2 \approx 0.82, 0.92, 0.99$ at $t_1 \approx 0.03\sqrt{\rho_d D_0^3/\gamma}$ and $F_2/\rho_d V_0^2 D_0^2 \approx 0.37, 0.337, 0.1$ at $t_2 \approx 0.42\sqrt{\rho_d D_0^3/\gamma}$, characterize the inertial shock from impact and the Worthington jet before takeoff, respectively. The drop reaches the maximum spreading at t_{\max} when it momentarily stops and retracts until $0.8\sqrt{\rho_d D_0^3/\gamma}$ when the drop takes off ($F = 0$). The black and gray dashed lines in panel (a) mark $F = 0$ and the resolution $F = 0.5 \text{ mN}$ of our piezoelectric force transducer, respectively. (b) Four instances are further elaborated through numerical simulations for ($We = 40, Oh = 0.0025$), namely (i) $t = 0 \text{ ms}$ (touch-down), (ii) $t = 0.37 \text{ ms}$ (t_1), (iii) $t = 2.5 \text{ ms}$ (t_{\max}), and (iv) $t = 4.63 \text{ ms}$ (t_2). The insets of panel (a) exemplify these four instances for the three representative cases illustrated here. The experimental snapshots are overlaid with the drop boundaries from simulations. We stress the excellent agreement between experiments and simulations without any free parameters. The left part of each numerical snapshot shows the dimensionless local viscous dissipation function $\tilde{\xi}_\eta \equiv \xi_\eta D_0 / (\rho_d V_0^3) = 2Oh (\tilde{\mathcal{D}} : \tilde{\mathcal{D}})$, where, \mathcal{D} is the symmetric part of the velocity gradient tensor, on a \log_{10} scale and the right part the velocity field magnitude normalized with the impact velocity. The black velocity vectors are plotted in the center of mass reference frame of the drop to clearly elucidate the internal flow. Also see supplementary videos SM1-SM3.

and capillary oscillations, offering insights into how viscosity affects the drop's behavior upon impact,

$$Oh = \frac{\eta_d}{\sqrt{\rho_d \gamma D_0}}. \quad (1.2)$$

Additionally, the Bond number

$$Bo = \frac{\rho_d g D_0^2}{\gamma} \quad (1.3)$$

57 compares gravity to inertial forces and is needed to uniquely define the non-dimensional
 58 problem.

59 The drop impact is not only interesting from the point of view of fundamental research
 60 but also finds relevance in inkjet printing (Lohse 2022), the spread of respiratory drops
 61 carrying airborne microbes (Bourouiba 2021; Ji *et al.* 2021; Pöhlker *et al.* 2023), cooling
 62 applications (Kim 2007; Shiri & Bird 2017; Jowkar & Morad 2019), agriculture (Bergeron
 63 *et al.* 2000; Bartolo *et al.* 2007; Kooij *et al.* 2018; Sijs & Bonn 2020; He *et al.* 2021;
 64 Hoffman *et al.* 2021), criminal forensics (Smith *et al.* 2018; Smith & Brutin 2018), and
 65 many other industrial and natural processes (Rein 1993; Yarin 2006; Tuteja *et al.* 2007;
 66 Cho *et al.* 2016; Josserand & Thoroddsen 2016; Yarin *et al.* 2017; Liu *et al.* 2017; Hao
 67 *et al.* 2016; Yarin *et al.* 2017; Wu *et al.* 2020). For these applications, it is pertinent to
 68 understand the forces involved in drop impacts, as these forces can lead to soil erosion
 69 (Nearing *et al.* 1986) or damage to engineered surfaces (Ahmad *et al.* 2013; Amirzadeh
 70 *et al.* 2017; Gohardani 2011). We refer the readers to Cheng *et al.* (2022) for an overview
 71 of the recent studies unraveling drop impact forces; see also Li *et al.* (2014); Soto *et al.*
 72 (2014); Philippi *et al.* (2016); Zhang *et al.* (2017); Gordillo *et al.* (2018); Mitchell *et al.*
 73 (2019); Zhang *et al.* (2019).

74 These forces have been studied by Zhang *et al.* (2022), employing experiments and
 75 simulations and deriving scaling laws. A liquid drop impacting a non-wetting substrate
 76 (figure 2i-vi) undergoes a series of phases—spreading, recoiling, and potentially rebounding
 77 (Chantelot 2018)—driven by the normal reaction force exerted by the substrate. The
 78 moment of touch-down (figure 2i-ii) (Wagner 1932; Philippi *et al.* 2016; Gordillo *et al.*
 79 2018) is not surprisingly associated with a pronounced peak in the temporal evolution of
 80 the drop impact force $F(t)$ owing to the sudden deacceleration as high as 100 times the
 81 acceleration due to gravity (Clanet *et al.* 2004) (figure 2, $F(t = 0.37\text{ ms}) \approx 5.1\text{ mN}$). The
 82 force diminishes as the drop reaches its maximum spreading diameter (figure 2iii). Zhang
 83 *et al.* (2022) revealed that also the jump-off is accompanied by a peak in the normal
 84 reaction force, which was up to then unknown (figure 2, $F_2(t_2 = 4.63\text{ ms}) \approx 2.3\text{ mN}$
 85 for the second force peak amplitude—at time t_2 after impact). The second peak in the
 86 force also coincides with the formation of a Worthington jet, a narrow upward jet of
 87 liquid that can form due to flow focusing by the retracting drop (figure 2iv-vi). Under
 88 certain conditions ($We \approx 9$), this peak can be even more pronounced than the first. This
 89 discovery is critical for superhydrophobicity which is volatile and can fail due to external
 90 disturbances such as pressure (Lafuma & Quéré 2003; Callies & Quéré 2005; Sbragaglia
 91 *et al.* 2007; Li *et al.* 2017), evaporation (Tsai *et al.* 2010; Chen *et al.* 2012; Papadopoulos
 92 *et al.* 2013), mechanical vibration (Bormashenko *et al.* 2007), or the impact forces of
 93 prior droplets (Bartolo *et al.* 2006a).

94 In contrast to our prior study Zhang *et al.* (2022), which fixed the Ohnesorge number
 95 to that of a 2 mm diameter water drop ($Oh = 0.0025$), our present investigation reported
 96 in this paper explores a broader parameter space. We systematically and independently
 97 vary the Weber and Ohnesorge numbers, extending the range of Oh to as high as 100.
 98 This comprehensive approach enables us to develop new scaling laws and provides a
 99 more unified understanding of the forces involved in drop impact problems. Our findings
 100 are particularly relevant for applications with varying viscosities and impact velocities
 101 (figure 1).

102 The structure of this paper is as follows: §2 briefly describes the experimental and
 103 numerical methods. §3 and §4 offer detailed analyses of the first and second peaks,
 104 respectively, focusing on their relationships with the Weber number (We) and the
 105 Ohnesorge number (Oh). Conclusions and perspectives for future research are presented
 106 in Section 5.

glycerol (wt %)	ρ_d (kg/m ³)	η_d (mPa.s)	γ (mN/m)
0	1000	1	72
50	1124	5	61
63	1158	10	61
74	1188	25.3	61
80	1200	45.4	61
85	1220	80.2	61

TABLE 1. Properties of the water-glycerol mixtures used in the experiments. ρ_d and η_d are the density and viscosity of the drop, respectively and γ denotes the liquid-air surface tension coefficient. These properties are calculated using the protocol provided in Cheng (2008); Volk & Kähler (2018).

107 2. Methods

108 2.1. Experimental method

109 In the experimental setup, shown schematically in figure 1(a), a liquid drop impacts a
110 superhydrophobic substrate. For water drops, such a surface is coated with silanized silica
111 nanobeads with a diameter of 20 nm (Glaco Mirror Coat Zero; Soft99) resulting in the
112 advancing and receding contact angles of $167 \pm 2^\circ$ and $154 \pm 2^\circ$, respectively (Gauthier
113 *et al.* 2015; Li *et al.* 2017). On the other hand, for viscous aqueous glycerin drops,
114 the upper surface is coated with an acetone solution of hydrophobic beads (Ultra ever
115 Dry, Ultratech International, a typical bead size of 20 nm), resulting in the advancing
116 and receding contact angles of $166 \pm 4^\circ$ and $159 \pm 2^\circ$, respectively (Jha *et al.* 2020).
117 The properties of the impacting drop are controlled using water-glycerol mixtures with
118 viscosities η_d varying by almost two orders of magnitude, from 1 mPas to 80.2 mPas,
119 yet maintaining a fairly constant surface tension γ and density ρ_d around 61 mN/m
120 and 1000 kg/m³, respectively (Cheng 2008; Volk & Kähler 2018; Jha *et al.* 2020). Using
121 other liquids like silicone oil could allow for a wider viscosity variation if used with
122 a superamphiphobic substrate (Deng *et al.* 2012). The drop diameter D_0 is controlled
123 between 2.05 mm and 2.76 mm by pushing it through a calibrated needle (see appendix A
124 for details). Consequently, changing the viscosity of the drop determines the Ohnesorge
125 number (Oh , see (1.2)). The Weber number (We , see (1.1)) is set using the impact velocity
126 V_0 varying between 0.38 m/s and 2.96 m/s by changing the release height of the drops
127 above the substrate. All experiments are conducted at ambient pressure and temperature.
128 The impact force is directly measured using a high-precision piezoelectric force transducer
129 (Kistler 9215A) with a resolution of 0.5 mN. During these measurements, the high-
130 frequency vibrations induced by the measurement system and the surrounding noise
131 are spectrally removed using a low pass filter with a cut-off frequency of 5 kHz, following
132 the procedure in Li *et al.* (2014); Zhang *et al.* (2017); Gordillo *et al.* (2018); Mitchell *et al.*
133 (2019). The experiment also employs a high-speed camera (Photron Fastcam Nova S12)
134 synchronized at 10,000 fps with a shutter speed 1/20,000 s. Throughout the manuscript,
135 the error bars account for repeated trials and are visible if they are larger than the
136 marker size. We refer the readers to the supplementary material of Zhang *et al.* (2022)
137 and appendix A for further details of the experimental setup and error characterization
138 of the dimensionless control parameters, respectively.

139 2.2. Numerical framework

140 In the direct numerical simulations (DNS) employed for this study, the continuity and
 141 the momentum equations take the form

$$\nabla \cdot \mathbf{v} = 0 \quad (2.1)$$

142 and

$$\frac{\partial \mathbf{v}}{\partial t} + \nabla \cdot (\mathbf{v} \mathbf{v}) = \frac{1}{\rho} (-\nabla p + \nabla \cdot (2\eta \mathcal{D}) + \mathbf{f}_\gamma) + \mathbf{g}, \quad (2.2)$$

143 respectively. Here, \mathbf{v} is the velocity field, t is time, p is pressure, and \mathbf{g} is acceleration
 144 due to gravity. We use the free software program *Basilisk C* that employs the well-
 145 balanced geometric volume of fluid (VoF) method (Popinet 2009, 2018). The VoF tracer
 146 Ψ delineates the interface between the drop (subscript d , $\psi = 1$) and air (subscript a ,
 147 $\psi = 0$), introducing a singular force $\mathbf{f}_\gamma \approx \gamma\kappa\nabla\Psi$ (κ denotes interfacial curvature, see
 148 Brackbill *et al.* 1992) to respect the dynamic boundary condition at the interface. This
 149 VoF tracer sets the material properties such that density ρ and viscosity η are given by

$$\rho = \rho_a + (\rho_d - \rho_a)\Psi \quad (2.3)$$

150 and

$$\eta = \eta_a + (\eta_d - \eta_a)\Psi, \quad (2.4)$$

151 respectively. This VoF field is advected with the flow, following the equation

$$\frac{\partial \Psi}{\partial t} + \nabla \cdot (\mathbf{v}\Psi) = 0. \quad (2.5)$$

152 Lastly, we calculate the normal reaction force $\mathbf{F}(t)$ by integrating the pressure field p at
 153 the substrate,

$$\mathbf{F}(t) = \left(\int_{\mathcal{A}} (p - p_0) d\mathcal{A} \right) \hat{\mathbf{z}}, \quad (2.6)$$

154 where, p_0 , $d\mathcal{A}$, and $\hat{\mathbf{z}}$ are the ambient pressure, substrate area element, and the unit
 155 vector normal to the substrate, respectively.

156 We leverage the axial symmetry of the drop impact (figure 1a). This axial symmetry
 157 breaks at large We (≥ 100 for water drops and even larger Weber number for more
 158 viscous drops), owing to destabilization by the surrounding gas after splashing (Xu *et al.*
 159 2005; Eggers *et al.* 2010; Driscoll & Nagel 2011; Riboux & Gordillo 2014; Josserand &
 160 Thoroddsen 2016; Zhang *et al.* 2022). To solve the governing equations (2.1)–(2.5), the
 161 velocity field \mathbf{v} and time t are normalized by the inertio-capillary scales, $V_\gamma = \sqrt{\gamma/\rho_d D_0}$
 162 and $\tau_\gamma = \sqrt{\rho_d D_0^3/\gamma}$, respectively. Furthermore, the pressure is normalized using the
 163 capillary pressure scale $p_\gamma = \gamma/D_0$. In such a conceptualization, Oh and We described in
 164 §1 uniquely determine the system. The Ohnesorge number based on air viscosity $Oh_a =$
 165 $(\eta_a/\eta_d)Oh$ and air-drop density ratio ρ_a/ρ_d are fixed at 10^{-5} and 10^{-3} , respectively
 166 to minimize the influence of the surrounding medium on the impact forces. Lastly, we R2
 167 keep the Bond number (Bo , see (1.3)) fixed at 1 throughout the manuscript. In our

system, the relevance of gravity is characterized by the dimensionless Froude number $Fr = V_0^2/gD_0 = We/Bo$ comparing inertia with gravity. Throughout this manuscript, $Fr > 1$ and gravity's role is sub-dominant compared to inertia (for detailed discussion, see appendix B). The substrate is modeled as a no-slip and non-penetrable wall, whereas vanishing stress and pressure are applied at the remaining boundaries to mimic outflow conditions for the surrounding air. The domain boundaries are far enough from the drop not to influence its impact process ($\mathcal{L}_{\max} \gg D_0$, $\mathcal{L}_{\max} = 8R$ in the worst case). At $t = 0$, in our simulations, we release a spherical drop (see appendix C) whose south pole is 0.05 D_0 away from the substrate and is falling with a velocity V_0 . The simulations utilize adaptive mesh refinement to finely resolve the velocity, viscous dissipation, and the VoF tracer fields. A minimum grid size $\Delta = D_0/2048$ is used for this study.

To ensure a perfectly non-wetting surface, we impose a thin air layer (minimum thickness $\sim \Delta/2$) between the drop and the substrate. This air layer prevents direct contact between the liquid and solid (Kolinski *et al.* 2014; Sprittles 2024), effectively mimicking a perfectly non-wetting surface. The presence of this air layer is crucial for capturing the dynamics of drop impact on superhydrophobic surfaces, as it allows for the formation of an air cushion that can significantly affect the spreading and rebound behavior of the drop (Ramírez-Soto *et al.* 2020; Sanjay *et al.* 2023a). While this approach does not fully resolve the microscopic dynamics within the air layer itself, such as the high-velocity gradients and viscous dissipation inside the gas film once it thins below a critical size ($\sim 10\Delta$), it has been shown to accurately capture the macroscopic behavior of drop impact in the parameter range of interest (Ramírez-Soto *et al.* 2020; Sanjay *et al.* 2023b; Alventosa *et al.* 2023a; García-Geijo *et al.* 2024). We refer the readers to Sanjay (2022) for discussions about this “precursor”, air film method and to Popinet & collaborators (2013–2023); Sanjay (2023); Zhang *et al.* (2022) for details on the numerical framework.

3. Anatomy of the first impact force peak

This section elucidates the anatomy of the first impact force peak and its relationship with the Weber We and Ohnesorge Oh numbers, first for the inertial limit (§3.1, $Oh \ll 1$) and then for the viscous asymptote (§3.2, $Oh \gg 1$). The results of this section are summarized in figure 3 that shows an excellent agreement between experiments and simulations without any free parameters.

3.1. Low Ohnesorge number impacts

For low Oh and large We , inertial force and time scales dictate the drop impact dynamics (figures 3 and 4). As the drop falls on a substrate, the part of the drop immediately in contact with the substrate stops moving, whereas the top of the drop still falls with the impact velocity (figure 4, from $t = t_1/4$ until $t = t_1$). Consequently, momentum conservation implies

$$F_1 \sim V_0 \frac{dm}{dt}, \quad (3.1)$$

where the mass flux $dm/dt \sim \rho_d V_0 D_0^2$ (Soto *et al.* 2014; Zhang *et al.* 2022). As a result, the first peak amplitude scales with the inertial pressure force (figure 3a)

$$F_1 \sim F_\rho, \text{ where } F_\rho = \rho_d V_0^2 D_0^2, \quad (3.2)$$

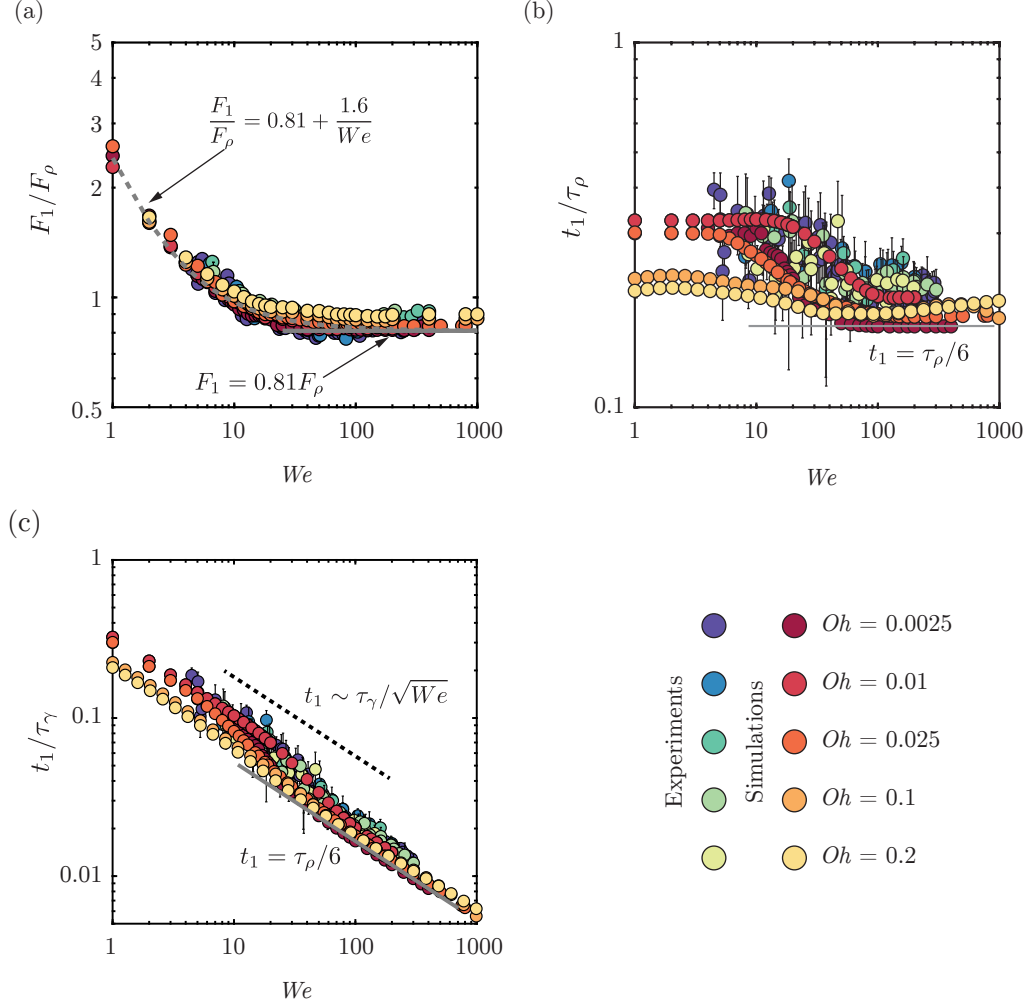


FIGURE 3. Anatomy of the first impact force peak amplitude at low Oh in between 0.0025 and 0.2, see color legend: We dependence of the (a) magnitude F_1 normalized by the inertial force scale $F_\rho = \rho_d V_0^2 D_0^2$ and time t_1 to reach the first force peak amplitude normalized by (b) the inertial timescale $\tau_\rho = D_0/V_0$ and (c) the inertia-capillary time scale $\tau_\gamma = \sqrt{\rho_d D_0^3/\gamma}$.

208 for high Weber numbers ($We > 30$, $F_1 \approx 0.81F_\rho$). Furthermore, the time t_1 to reach F_1
209 follows

$$t_1 \sim \frac{D_0}{V_0} = \tau_\rho, \quad (3.3)$$

210 where, τ_ρ is the inertial timescale. The relation between equations (3.2) and (3.3) is
211 apparent from the momentum conservation which implies that the impulse of the first
212 force peak is equal to the momentum of the impacting drop, i.e., $F_1 t_1 \sim \rho_d V_0 D_0^3 = F_\rho \tau_\rho$
213 (see Gordillo *et al.* 2018, Zhang *et al.* 2022, and figures 3b,c). These scaling laws depend
214 only on the inertial shock at impact and are wettability-independent (Zhang *et al.* 2017;
215 Gordillo *et al.* 2018; Zhang *et al.* 2022). For details of the scaling law, including the

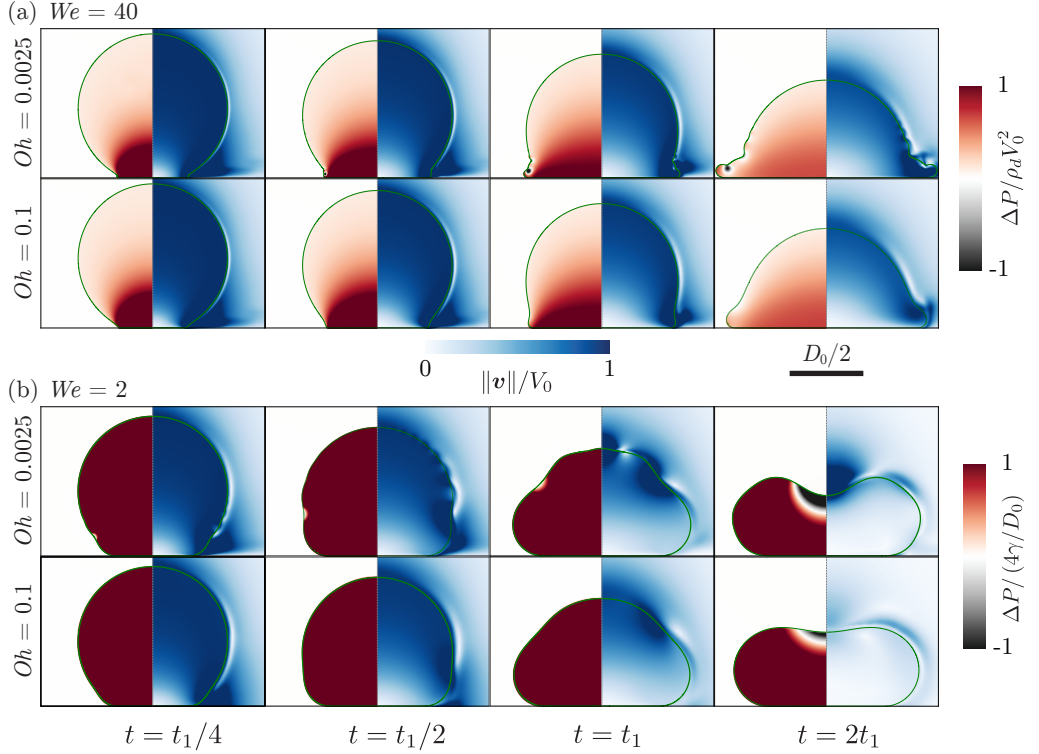


FIGURE 4. Direct numerical simulations snapshots illustrating the drop impact dynamics for $We = (a) 40$ and $(b) 2$. The left-hand side of each numerical snapshot shows the pressure normalized by (a) the inertial pressure scale $\rho_d V_0^2$ and (b) the capillary pressure scale γ/D_0 . The right-hand side shows the velocity field magnitude normalized by the impact velocity V_0 .

prefactors, we refer the readers to [Philippi et al. \(2016\)](#); [Gordillo et al. \(2018\)](#); [Cheng et al. \(2022\)](#).

[Figure 3](#) further illustrates that this inertial asymptote is insensitive to viscosity variations up to 100-fold as $F_1 \sim F_\rho$ and $t_1 \sim \tau_\rho$ for $0.0025 < Oh < 0.2$. However, deviations from the inertial force and time scales are apparent for $We < 30$ ([figure 3](#)), a phenomenon also reported in earlier work ([Soto et al. 2014](#); [Zhang et al. 2022](#)). In these instances, inertia does not act as the sole governing force but instead complements surface tension, which dictates the pressure inside the drop ($p \sim \gamma/D_0$ throughout the drop for $We \lesssim 1$, [figure 4b](#)). [Zhang et al. \(2022\)](#) proposed an empirical functional dependence as

$$F_1 = \left(\alpha_1 \rho_d V_0^2 + \alpha_2 \frac{\gamma}{D_0} \right) D_0^2, \quad (3.4)$$

based on dimensional analysis, with α_1 and α_2 as free parameters which were determined to be approximately 1.6 and 0.81, respectively for water ($Oh = 0.0025$). These coefficients only deviate marginally in the current work despite the significant increase in Oh as compared to previous works ([Cheng et al. 2022](#); [Zhang et al. 2022](#)). This consistency underscores the invariance of the pressure field inside the drop to an increase in Oh (close to the impact region, [figure 4a](#) and throughout the drop, [figure 4b](#)).

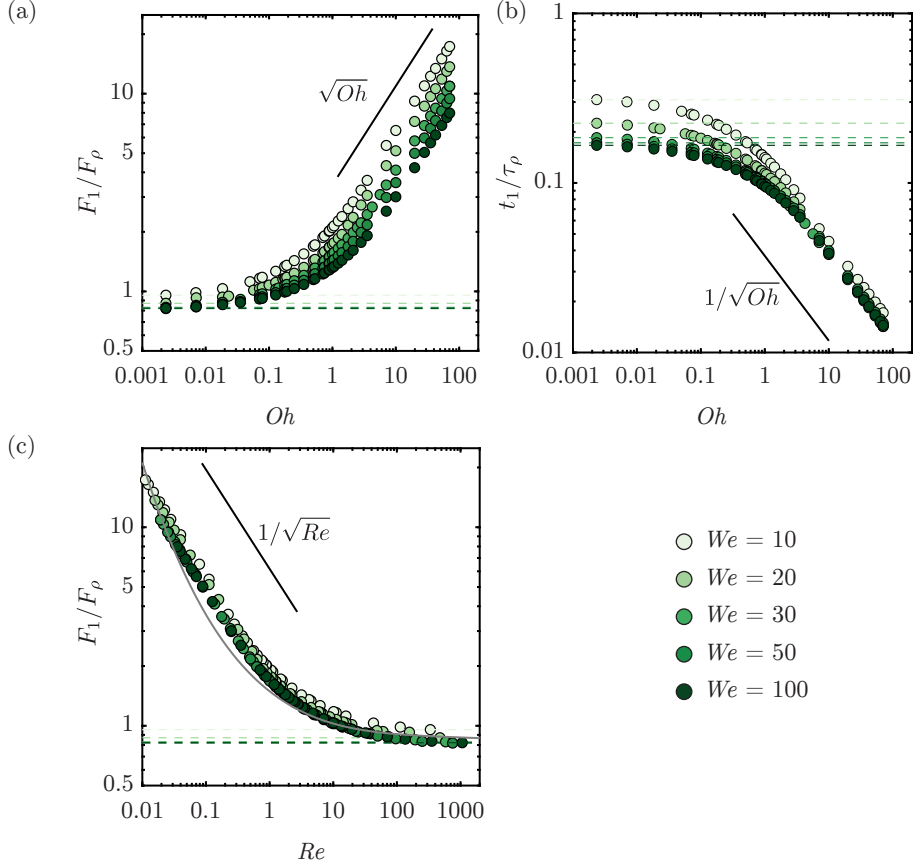


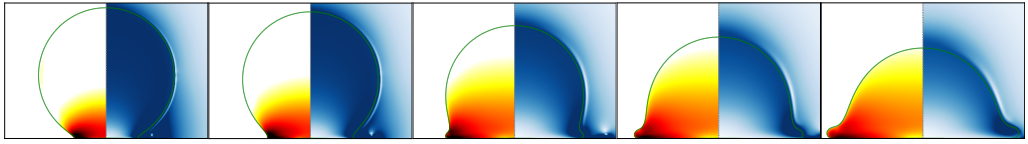
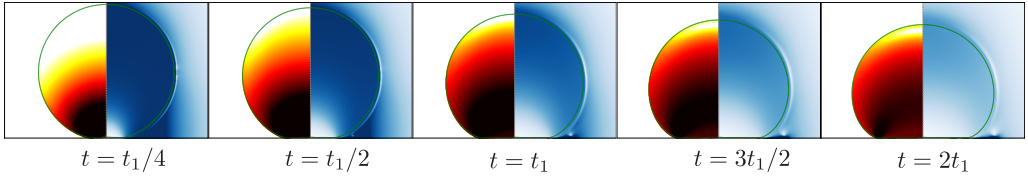
FIGURE 5. Anatomy of the first impact force peak amplitude for viscous impacts from our numerical simulations: the Oh dependence of (a) the magnitude F_1 normalized by the inertial force scale $\rho_d V_0^2 D_0^2$ and (b) the time t_1 to reach the first force peak amplitude normalized by inertial timescale $\tau_\rho = D_0/V_0$. (c) The Re dependence of the magnitude F_1 normalized by the inertial force scale $\rho_d V_0^2 D_0^2$ as compared to the (implicit) theoretical calculation of Gordillo *et al.* (2018). The black line corresponds to the scaling relationship described in §3.2. The Weber number is color-coded.

3.2. Large Ohnesorge number impacts

Figure 5 reaffirms the findings of §3.1 for low Oh that the first impact peak amplitude F_1 and the time to reach this peak amplitude t_1 scale with F_ρ and τ_ρ , respectively. As the Ohnesorge number increases further, the first impact force peak amplitude normalized with F_ρ begins to increase, indicating a transition around $Oh \approx 0.1$, where viscosity starts to play a significant role. At large Oh , we observe the scaling relationship (figure 5a)

$$F_1 \sim F_\rho \sqrt{Oh}. \quad (3.5)$$

The drop's momentum is still $\rho_d V_0 D_0^3$ which must be balanced by the impulse from the substrate, $F_1 t_1$ (see §3.1, Gordillo *et al.* 2018, Zhang *et al.* 2022, and figure 5b). Consequently, the time t_1 follows

(a) $Oh = 0.05$ (b) $Oh = 0.5$ (c) $Oh = 5$ 

$t = t_1/4 \quad t = t_1/2 \quad t = t_1 \quad t = 3t_1/2 \quad t = 2t_1$

$$\begin{array}{c} -3 \quad \log_{10} (\tilde{\xi}_\eta) \quad 0.5 \\ \hline D_0/2 \\ \hline 0 \quad \|v\|/V_0 \quad 1 \end{array}$$

FIGURE 6. Direct numerical simulations snapshots illustrating the drop impact dynamics for $We = 100$ and $Oh =$ (a) 0.05 , (b) 0.5 , and (c) 5 . The left-hand side of each numerical snapshot shows the viscous dissipation function $\tilde{\xi}_\eta$ normalized by the inertial scale $\rho_d V_0^3 / D_0$. The right-hand side shows the velocity field magnitude normalized by the impact velocity V_0 .

$$t_1 \sim \frac{\tau_\rho}{\sqrt{Oh}}. \quad (3.6)$$

Figure 5 further shows that these scaling laws are weakly dependent on the Weber number, as viscous dissipation consumes the entire initial kinetic energy of the impacting drop (figure 6). Once again, we stress that using the water-glycerol mixtures limits the range of Oh that we can probe experimentally. We further note that the first peak is robust and does not depend on the wettability of the substrate. Consequently, to compare with the existing data such as those in Cheng *et al.* (2022) with different liquids to cover a wider range of liquid viscosities and to account for the apparent We -dependence, we plot F_1 compensated with F_ρ against the impact Reynolds number $Re \equiv \sqrt{We}/Oh = V_0 D_0 / \nu_d$. For the low Re regime, such a plot allows us to describe the We dependence on the prefactor more effectively, as illustrated in figure 5(c). However, it is important to note that some scatter is still observed at high Re values, which can be attributed to the We dependence of the impact force peak amplitude. This lack of a pure scaling behavior demonstrates how the interplay between kinetic energy and viscous dissipation within the drop dictates the functional dependence of the maximum impact force on Oh .

To systematically elucidate these scaling behaviors in the limit of small Re , we need to find the typical scales for the rate of change of kinetic energy and that of the rate of viscous dissipation for the drop impact system. First, we can readily define an average rate of viscous dissipation per unit mass as

$$\bar{\varepsilon} \sim \frac{1}{\tau_\rho} \frac{1}{D_0^3} \int_0^{\tau_\rho} \int_{\Omega} \nu_d (\mathcal{D} : \mathcal{D}) d\Omega dt, \quad (3.7)$$

where ν_d is the kinematic viscosity of the drop and $d\Omega$ is the volume element where dissipation occurs. Notice that $\bar{\varepsilon}$ has the dimensions of V_0^3/D_0 , i.e., length squared over time cubed or velocity squared over time, as it should be for dissipation rate of energy per unit mass. We can estimate $\Omega = D_{\text{foot}}^2 l_\nu$ (figure 6), where D_{foot} is the drop's foot diameter in contact with the substrate and l_ν is the viscous boundary layer thickness. This boundary layer marks the region of strong velocity gradients ($\sim V_0/l_\nu$) analogous to the Mirels (1955) shockwave-induced boundary layer. For details, we refer the authors to Schlichting (1968); Schroll *et al.* (2010); Philippi *et al.* (2016). Consequently, the viscous dissipation rate scales as

$$\bar{\varepsilon} \sim \frac{1}{\tau_\rho D_0^3} \int_0^{\tau_\rho} \nu_d \left(\frac{V_0}{l_\nu} \right)^2 D_{\text{foot}}^2 l_\nu dt. \quad (3.8)$$

To calculate D_{foot} , we assume that the drop maintains a spherical cap shape throughout the impact (figure 6). To calculate the distance the drop would have traveled if there were no substrate, we use the relation $d \sim V_0 t$. Simple geometric arguments allow us to determine the relation between the foot diameter and this distance, $D_{\text{foot}} \sim \sqrt{D_0 d}$ (Lesser 1981; Mandre *et al.* 2009; Zheng *et al.* 2021; Bilotto *et al.* 2023; Bertin 2023). Interestingly, this scaling behavior is similar to the inertial limit (Wagner 1932; Bouwhuis *et al.* 2012; Philippi *et al.* 2016; Gordillo *et al.* 2019) as discussed by Langley *et al.* (2017); Bilotto *et al.* (2023). Furthermore, the viscous boundary layer l_ν can be approximated using $\sqrt{\nu_d t}$ (Mirels 1955; Eggers *et al.* 2010; Philippi *et al.* 2016). Filling these in (3.8), we get

$$\bar{\varepsilon} \sim \frac{1}{\tau_\rho D_0^2} \int_0^{\tau_\rho} \sqrt{\nu_d} V_0^3 \sqrt{t} dt, \quad (3.9)$$

which on integration gives

$$\bar{\varepsilon} \sim \sqrt{\nu_d \tau_\rho} V_0^3 / D_0^2, \quad (3.10)$$

where τ_ρ is the inertial time scale. Here, we assume that for highly viscous drops, all energy is dissipated within a fraction of τ_ρ . Filling in (3.10) and normalizing $\bar{\varepsilon}$ with the inertial scales V_0^3/D_0 ,

$$\frac{\bar{\varepsilon}}{V_0^3/D_0} \sim \sqrt{\frac{\nu_d \tau_\rho}{D_0^2}} = \frac{1}{\sqrt{Re}} = \left(\frac{Oh}{\sqrt{We}} \right)^{1/2}. \quad (3.11)$$

Next, the kinetic energy of the falling drop is given by

$$\dot{K}(t) \equiv \frac{dK(t)}{dt} \sim \rho_d D_0^3 \bar{\varepsilon}, \quad \text{where } K(t) = \frac{1}{2} m (V(t))^2, \quad (3.12)$$

and $V(t)$ is the drop's center of mass velocity. The left-hand side of (3.12) can be written as

$$\dot{K}(t) = mV(t) \frac{dV(t)}{dt} = F(t)V(t). \quad (3.13)$$

284 In equation (3.13), $F(t)$ and $V(t)$ scale with the first impact force peak amplitude F_1
 285 and the impact velocity V_0 , respectively, giving the typical scale of the rate of change of
 286 kinetic energy as

$$\dot{K}^* \sim F_1 V_0. \quad (3.14)$$

287 We stress that (3.14) states that the rate of change of kinetic energy is equal to the power
 288 of the normal reaction force, an observation already made by [Wagner \(1932\)](#) and [Philippi
 289 et al. \(2016\)](#) in the context of impact problems. Lastly, at large Oh , viscous dissipation
 290 enervates kinetic energy completely giving (figure 6c, also see: [Philippi et al. \(2016\)](#) and
 291 [Wildeman et al. \(2016\)](#)),

$$\dot{K}^* \sim F_1 V_0 \sim \rho_d D_0^3 \bar{\varepsilon} \quad (3.15)$$

292 Additionally, we use the inertial scales to non-dimensionalize (3.15) and fill in (3.11),
 293 giving

$$\frac{F}{F_\rho} \sim \frac{\bar{\varepsilon}}{V_0^3/D_0} \sim \frac{1}{\sqrt{Re}} = \left(\frac{Oh}{\sqrt{We}} \right)^{1/2} \quad (3.16)$$

294 and using $F_1 t_1 \sim \rho_d V_0 D_0^3 = F_\rho \tau_\rho$,

$$\frac{t_1}{\tau_\rho} \sim \left(\frac{\sqrt{We}}{Oh} \right)^{1/2}. \quad (3.17)$$

295 In summary, we use energy and momentum invariance to elucidate the parameter
 296 dependencies of the impact force as illustrated in figure 5. The scaling arguments
 297 capture the dominant force balance during the impact process, considering the relative
 298 importance of inertial, capillary, and viscous forces. As the dimensionless viscosity of
 299 impacting drops increases, the lack of surface deformation increases the normal reaction
 300 force (3.16). Further, the invariance of incoming drop momentum implies that this
 301 increase in normal reaction force occurs on a shorter timescale (3.17).

302 4. Anatomy of the second impact force peak

303 This section delves into the anatomy of the second impact force peak amplitude F_2 as a
 304 function of the Weber We and Ohnesorge Oh numbers, summarized in figure 7. We once
 305 again note the remarkable agreement between experiments and numerical simulations in
 306 this figure.

307 Similar to the mechanism leading to the formation of the first peak (§3), also the
 308 mechanism for the formation of this second peak is momentum conservation. As the
 309 drop takes off the surface, it applies a force on the substrate. As noted in §1 and [Zhang
 310 et al. \(2022\)](#), this force also coincides with the formation of a Worthington jet (figure 2iv-
 311 vi). The time t_2 at which the second peak is observed scales with the inertio-capillary
 312 timescale and is insensitive to We and Oh (figure 7b,c). Once again, we invoke the analogy

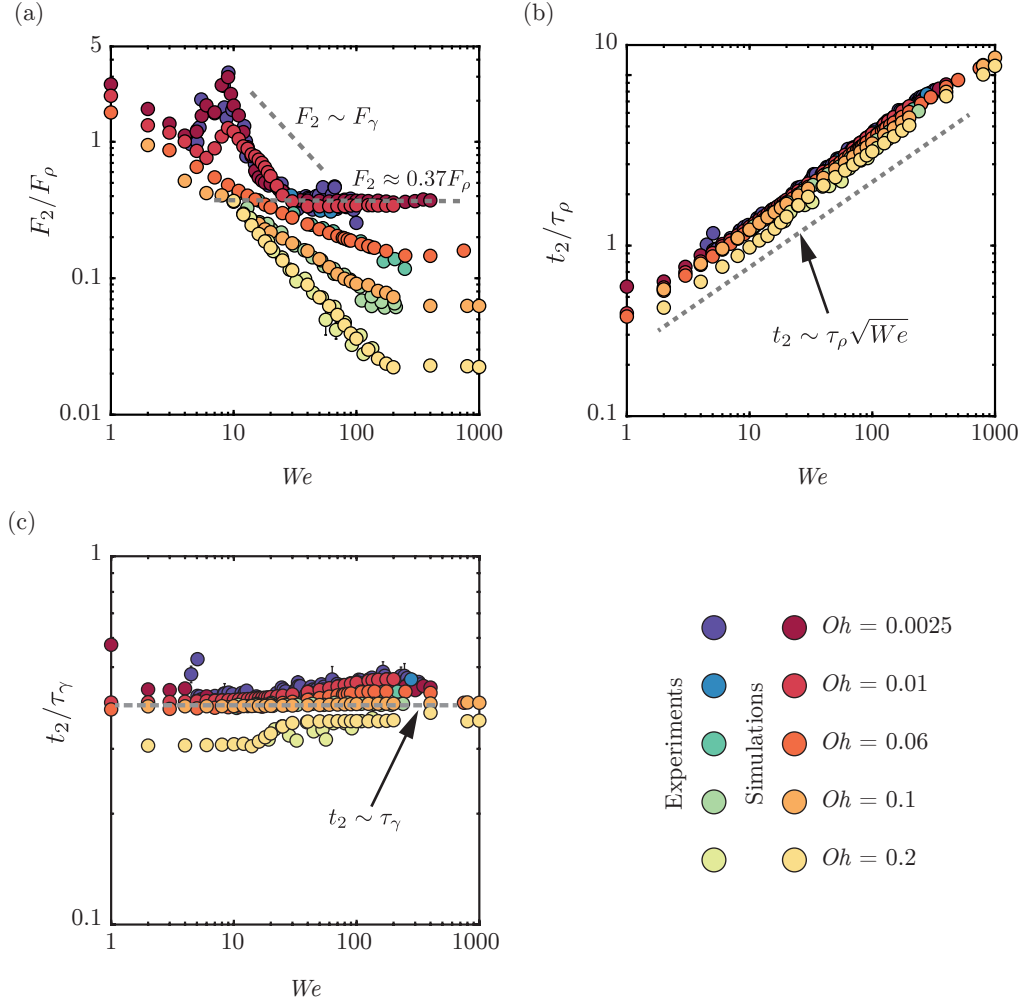


FIGURE 7. Anatomy of the second impact force peak amplitude: We dependence of the (a) magnitude F_2 normalized by the inertial force scale $F_\rho = \rho_d V_0^2 D_0^2$ and time t_2 to reach the second force peak amplitude normalized by (b) the inertio-capillary time scale $\tau_\gamma = \sqrt{\rho_d D_0^3 / \gamma}$ and (c) inertial timescale $\tau_\rho = D_0 / V_0$.

313 between drop oscillation and drop impact to explain this behavior (Richard *et al.* 2002;
 314 Chevy *et al.* 2012). At the time instant $t_2 \approx 0.44\tau_\gamma$, the drop's internal motion undergoes
 315 a transition from a predominantly radial flow to a vertical one due to the formation of
 316 the Worthington jet (Chantelot 2018; Zhang *et al.* 2022). Figure 8 exemplifies this jet in
 317 the $Oh - We$ parameter space, which is intricately related to the second peak in the drop
 318 impact force. For low Oh and large We , the drop retraction follows a modified Taylor-
 319 Culick dynamics (Bartolo *et al.* 2005; Eggers *et al.* 2010; Sanjay *et al.* 2022). As We is
 320 increased, the jet gets thinner but faster, maintaining a constant momentum flux $\rho_d V_j^2 d_j^2$,
 321 where V_j and d_j are the jet's velocity and diameter, respectively (figure 8, Zhang *et al.*
 322 2022). This invariance leads to the observed scaling $F_2 \sim F_\rho$ in this regime ($F_2 \approx 0.37F_\rho$
 323 for $We \geq 30, Oh \leq 0.01$).

324 Furthermore, the low We and Oh regime relies entirely on capillary pressure (figure 4).

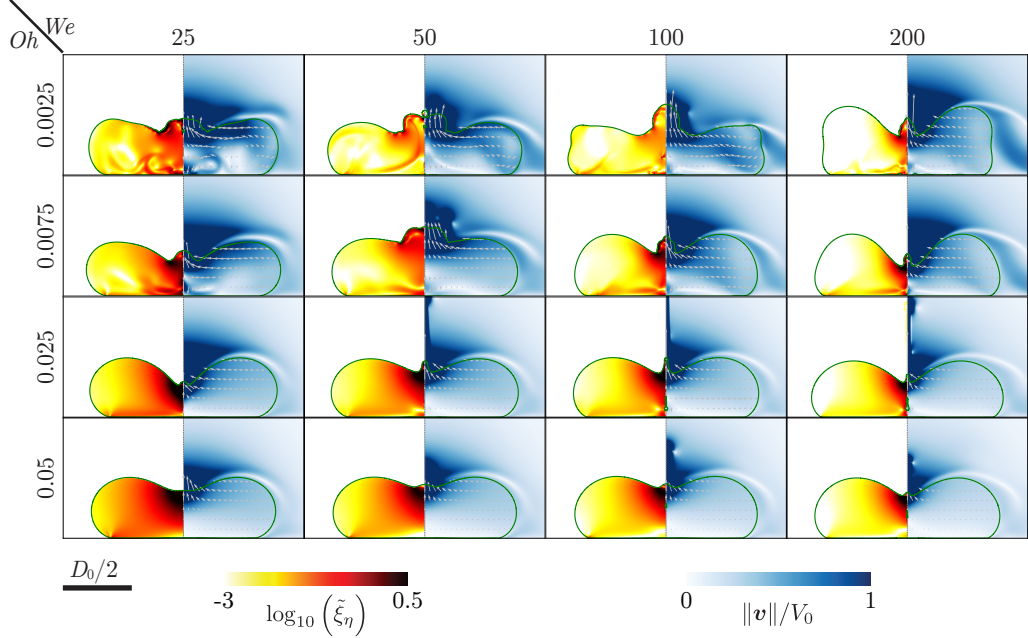


FIGURE 8. Direct numerical simulations snapshots illustrating the influence of We and Oh on the inception of the Worthington jet. All these snapshots are taken at the instant when the second peak appears in the temporal evolution of the normal reaction force ($t = t_2$). The left-hand side of each numerical snapshot shows the viscous dissipation function ξ_η normalized by the inertial scale $\rho_d V_0^3 / D_0$. The right-hand side shows the velocity field magnitude normalized by the impact velocity V_0 . The gray velocity vectors are plotted in the center of mass reference frame of the drop to clearly elucidate the internal flow.

Subsequently, $F_2 \sim F_\gamma = \gamma D_0$ for $Oh < 0.01$ and $We < 30$ (figure 7). This flow focusing (figure 8) is most efficient for $We = 9$ (figure 9a, $t_2/2 < t < t_2$, Renard *et al.* 2003; Bartolo *et al.* 2006b) where the capillary resonance leads to a thin-fast jet, accompanied by a bubble entrainment, reminiscent of the hydrodynamic singularity (figure 9, Zhang *et al.* 2022; Sanjay *et al.* 2021). The characteristic feature of this converging flow is a higher magnitude of F_2 compared to F_1 (figure 7).

However, this singular jet regime is very narrow in the $Oh - We$ phase space. Figure 9b shows two cases for water drops ($Oh = 0.0025$) at different We (5 and 12 for figures 9b-i and b-ii, respectively). Bubble entrainment does not occur in either of these cases. Consequently, the maximum force amplitude diminishes for these two cases (figure 7). Nonetheless, these cases are still associated with high local viscous dissipation near the axis of symmetry owing to the singular nature of the flow. Another mechanism to inhibit this singular Worthington jet is viscous dissipation in the bulk. As the Ohnesorge number increases, this singular jet formation disappears ($Oh = 0.005$, figure 9c-i), significantly reducing the second peak of the impact force. For even higher viscosities, the drop no longer exhibits the sharp, focused jet formation seen at lower viscosities, and the second peak in the force is notably diminished ($Oh = 0.05$, figure 9c-ii).

Lastly, as Oh increases, bulk dissipation becomes dominant (apparent from increasing Oh at fixed We in figure 8) and can entirely inhibit drop bouncing. Recently, Jha *et al.* (2020); Sanjay *et al.* (2023a) showed that there exists a critical Oh , two orders of magnitude higher than that of a 2 mm diameter water drop, beyond which drops do not bounce either, irrespective of their impact velocity. Consequently, the second peak

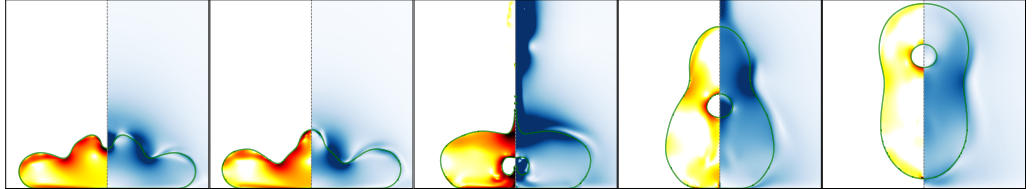
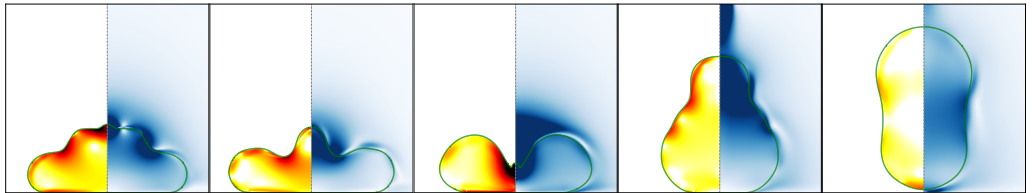
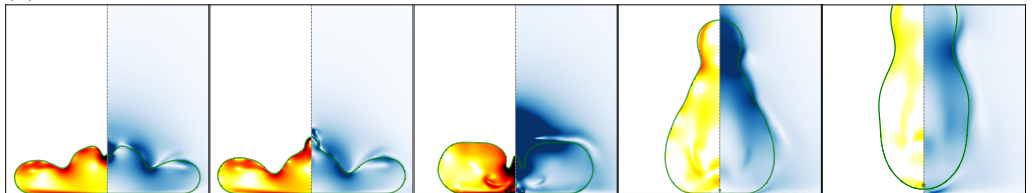
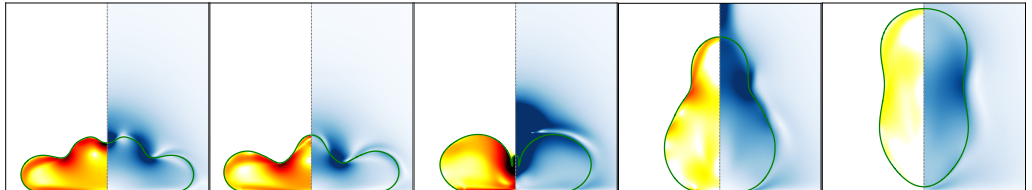
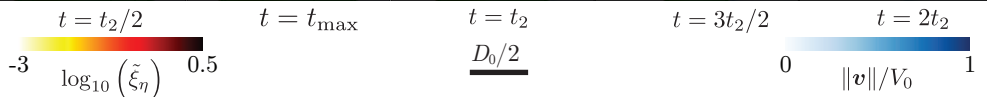
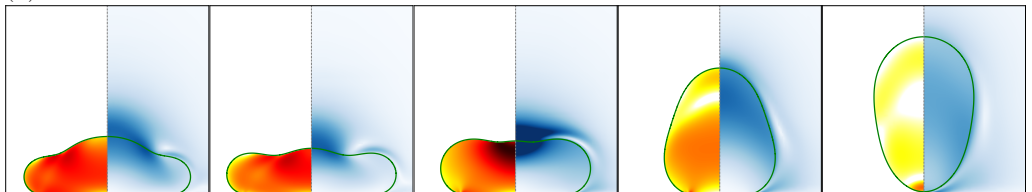
(a) $We = 9, Oh = 0.0025$ (b) $Oh = 0.0025$ (i) $We = 5$ (ii) $We = 12$ (c) $We = 9$ (i) $Oh = 0.005$ (ii) $Oh = 0.05$ 

FIGURE 9. Direct numerical simulations snapshots illustrating the influence of We and Oh on the singular Worthington jet. (a) $(We, Oh) = (9, 0.0025)$, (b) $Oh = 0.0025$ with $We =$ (i) 5 and (ii) 12, and (c) $We = 9$ with $Oh =$ (i) 0.005 and (ii) $Oh = 0.05$. The left-hand side of each numerical snapshot shows the viscous dissipation function ξ_η normalized by inertial scale $\rho_d V_0^3 / D_0$. The right-hand side shows the velocity field magnitude normalized by the impact velocity V_0 .

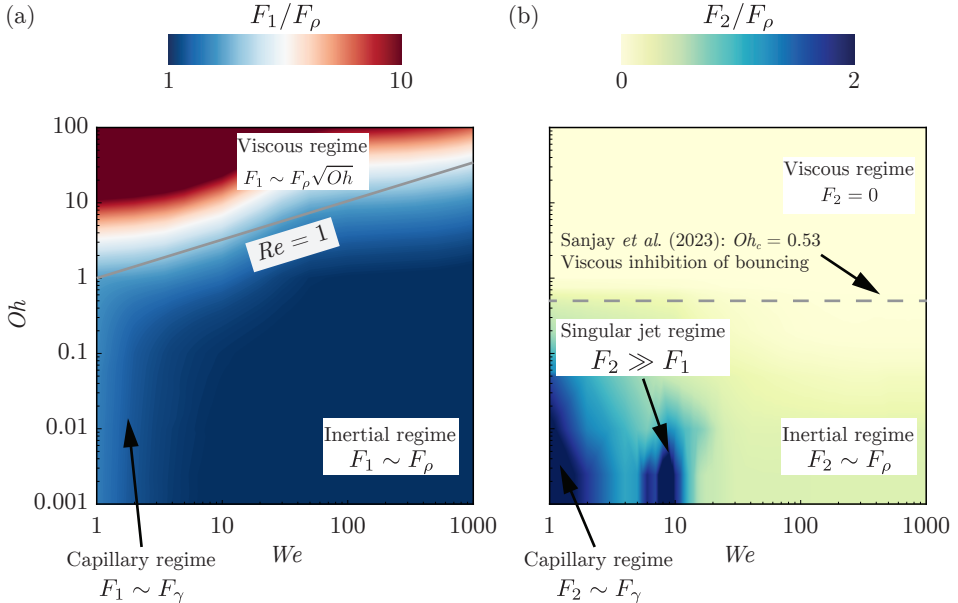


FIGURE 10. Regime map in terms of the drop Ohnesorge number Oh and the impact Weber number We to summarize the two peaks in the impact force by showing the different regimes described in this work based on (a) the first peak in the impact force peak amplitude F_1 and (b) the second peak in the impact force peak amplitude F_2 . Both peaks are normalized by the inertial force scale $F_\rho = \rho_d V_0^2 D_0^2$. These regime maps are constructed using ~ 1500 simulations in the range $0.001 \leq Oh \leq 100$ and $1 \leq We \leq 1000$. The gray solid line in (a) and dashed line in (b) mark the inertial-viscous transition ($Re = 1$) and the bouncing-no-bouncing transition ($Oh_c = 0.53$ for $Bo = 1$, see Sanjay et al. (2023a)), respectively.

in the impact force diminishes for larger Oh , which explains the monotonic decrease of the amplitude F_2 observed in figure 7 for $We > 30, Oh > 0.01$.

5. Conclusion and outlook

In this work, we study the forces and dissipation encountered during the drop impact process by employing experiments, numerical simulations, and theoretical scaling laws. We vary the two dimensionless control parameters—the Weber (We : dimensionless impact velocity) and the Ohnesorge number (Oh : dimensionless viscosity) independently to elucidate the intricate interplay between inertia, viscosity, and surface tension in governing the forces exerted by a liquid drop upon impact on a non-wetting substrate.

For the first impact force peak amplitude F_1 , owing to the momentum balance after the inertial shock at impact, figure 10(a) summarizes the different regimes in the Oh — We phase space. For low Oh , inertial forces predominantly dictate the impact dynamics, such that F_1 scales with the inertial force F_ρ (Philippi et al. 2016; Gordillo et al. 2018; Mitchell et al. 2019; Cheng et al. 2022; Zhang et al. 2022) and is insensitive to viscosity variations up to 100-fold. As Oh increases, the viscosity becomes significant, leading to a new scaling law: $F_1 \sim F_\rho \sqrt{Oh}$. The paper unravels this viscous scaling behavior by accounting for the loss of initial kinetic energy owing to viscous dissipation inside the drop. Lastly, at low We , the capillary pressure inside the drop leads to the scaling $F_1 \sim F_\gamma$ (Moláček & Bush 2012; Chevy et al. 2012).

The normal reaction force described in this work is responsible for deforming the drop as it spreads onto the substrate, where it stops thanks to surface tension. If the

substrate is non-wetting, it retracts to minimize the surface energy and finally takes off (Richard & Quéré 2000). In this case, the momentum conservation leads to the formation of a Worthington jet and a second peak in the normal reaction force, as summarized in figure 10(b). For low Oh and high We , the second force peak amplitude scales with the inertial force (F_ρ), following a modified Taylor-Culick dynamics (Eggers *et al.* 2010). In contrast, capillary forces dominate at low We and low Oh , leading to a force amplitude scaling of $F_2 \sim F_\gamma$. We also identify a narrow regime in the $Oh - We$ phase space where a singular Worthington jet forms, significantly increasing F_2 (Bartolo *et al.* 2006b; Zhang *et al.* 2022), localized in the parameter space for $We \approx 9$ and $Oh < 0.01$. As Oh increases, bulk viscous dissipation counteracts this jet formation, diminishing the second peak and ultimately inhibiting drop bouncing.

Our findings have far-reaching implications, not only enriching the fundamental understanding of fluid dynamics of drop impact but also informing practical applications in diverse fields such as inkjet printing, public health, agriculture, and material science where the entire range of $Oh - We$ phase space is relevant (figures 1b and 10). While this has identified new scaling laws, it also opens avenues for future research. For instance, it would be interesting to use the energy accounting approach to unify the scaling laws for the maximum spreading diameter for arbitrary Oh (Laan *et al.* 2014; Wildeman *et al.* 2016). Although, the implicit theoretical model summarized in Cheng *et al.* (2022) describes most of data in figure 5, we stress the importance of having a predictive model to determine F_1 for given We and Oh (Sanjay & Lohse 2024). The We influence on the impact force also warrants further exploration, especially in the regime $We \ll 1$ for arbitrary Oh (Chevy *et al.* 2012; Moláček & Bush 2012) and drop impact on compliant surfaces (Alventosa *et al.* 2023b; Ma & Huang 2023). Another potential extension of this work is to non-Newtonian fluids (Martouzet *et al.* 2021; Agüero *et al.* 2022; Bertin 2023; Jin *et al.* 2023).

394

Code availability. The codes used in the present article are permanently available at Sanjay (2023).

397

Acknowledgements. We would like to thank Vincent Bertin for comments on the manuscript. We would also like to thank Andrea Prosperetti, Pierre Chantelot, Devaraj van der Meer, and Uddalok Sen for illuminating discussions.

401

Funding. We acknowledge the funding by the ERC Advanced Grant No. 740479-DDD and NWO-Canon grant FIP-II. B.Z and C.L are grateful for the support from National Natural Science Foundation of China (Grant No. 12172189, 11921002, 11902179). This work was carried out on the national e-infrastructure of SURFsara, a subsidiary of SURF cooperation, the collaborative ICT organization for Dutch education and research. This work was sponsored by NWO - Domain Science for the use of supercomputer facilities.

408

Declaration of Interests. The authors report no conflict of interest.

410

Author ORCID.

V. Sanjay <https://orcid.org/0000-0002-4293-6099>;

B. Zhang <https://orcid.org/0000-0001-8550-2584>;

C. Lv <https://orcid.org/0000-0001-8016-6462>;

414

415 D. Lohse <https://orcid.org/0000-0003-4138-2255>.

416

417 Appendix A. Note on the parametric error characterization

418 This appendix outlines the methodology for characterizing experimental errors in quantification of the drop's size and impact velocities which is crucial for accurate calculation
 419 of dimensionless control parameters, We and Oh . The drop diameter determination
 420 involves multiple steps. First, we measure the total mass (M_{100}) of 100 drops using an
 421 electric balance. From this mass, using the liquid density and assuming spherical shape,
 422 we calculated the drop diameter (D_0). We repeated this process five times, yielding
 423 $D_{0,1}$ through $D_{0,5}$. The average of these measurements provided the final drop diameter
 424 (D_0) and its standard error. For impact velocity determination, we extracted data from
 425 experimental high-speed imagery. By tracking the drop center's position in successive
 426 frames prior to substrate contact, and knowing the frame rate, we calculated the impact
 427 velocity. We repeated this process for five trials, obtaining $V_{0,1}$ through $V_{0,5}$. The average
 428 of these values gave the final impact velocity (V_0) and its standard error.

429 The standard errors for drop diameters do not exceed 0.13 mm. For instance, drops with
 430 Ohnesorge numbers of 0.0025, 0.0625, and 0.2 have diameters of 2.05 ± 0.13 mm, $2.52 \pm$
 431 0.11 mm, and 2.54 ± 0.09 mm, respectively. The standard errors for impact velocities did
 432 not exceed 0.02 m/s. For the same Oh values, the impact velocities were 1.2 ± 0.002 m/s,
 433 0.97 ± 0.01 m/s, and 0.96 ± 0.01 m/s, respectively. The combined errors in D_0 and V_0
 434 resulted in approximately $\pm 7\%$ error in Weber number We and $\pm 3\%$ error in Ohnesorge
 435 number Oh . Consequently, the horizontal error bars, which relate to errors in the control
 436 parameters, are smaller than the symbol sizes in our figures.

438 Appendix B. Role of gravity on drop impact forces

439 Appendix C. Role of drop shape on impact forces

440 It is important to note that the drops may not be perfectly spherical and may have
 441 residual oscillations as they are released from the needle and arrive at the substrate.
 442 These oscillations are expected to be more pronounced for cases with small Weber and
 443 Ohnesorge numbers. The exact shape of the drop just before impact can influence the
 444 impact dynamics (Thoraval *et al.* 2013; Yun 2017). However, we suspect that the influence
 445 of these shape variations is captured, at least in part, by the error bars in the experimental
 446 data, which are derived from repeated trials under the same nominal conditions.

REFERENCES

- 447 AGÜERO, E. A., ALVENTOSA, L. F. L., HARRIS, D. M. & GALEANO-RIOS, C. A. 2022 Impact
 448 of a rigid sphere onto an elastic membrane. *Proc. R. Soc. Lond. A* **478** (2266), 20220340.
- 449 AHMAD, M., SCHATZ, M. & CASEY, M. V. 2013 Experimental investigation of droplet size
 450 influence on low pressure steam turbine blade erosion. *Wear* **303**, 83–86.
- 451 ALVENTOSA, L. F. L., CIMPEANU, R. & HARRIS, D. M. 2023a Inertio-capillary rebound of a
 452 droplet impacting a fluid bath. *J. Fluid Mech.* **958**, A24.
- 453 ALVENTOSA, L. F. L., CIMPEANU, R. & HARRIS, D. M. 2023b Inertio-capillary rebound of a
 454 droplet impacting a fluid bath. *J. Fluid Mech.* **958**, A24.
- 455 AMIRZADEH, B., LOUGHALAM, A., RAESSI, M. & TOOTKABONI, M. 2017 A computational
 456 framework for the analysis of rain-induced erosion in wind turbine blades. *J. Wind Eng.*
 457 *Ind. Aerodyn.* **163**, 33–43.
- 458 BARTOLO, D., BOUAMRIRENE, F., VERNEUIL, E., BUGUIN, A., SILBERZAN, P. & MOULINET,

- 459 S. 2006a Bouncing or sticky droplets: Impalement transitions on superhydrophobic
460 micropatterned surfaces. *Europhys. Lett.* **74** (2), 299.
- 461 BARTOLO, D., BOUDAOU, A., NARCY, G. & BONN, D. 2007 Dynamics of non-Newtonian
462 droplets. *Phys. Rev. Lett.* **99** (17), 174502.
- 463 BARTOLO, D., JOSSERAND, C. & BONN, D. 2005 Retraction dynamics of aqueous drops upon
464 impact on non-wetting surfaces. *J. Fluid Mech.* **545**, 329–338.
- 465 BARTOLO, D., JOSSERAND, C. & BONN, D. 2006b Singular jets and bubbles in drop impact.
466 *Phys. Rev. Lett.* **96** (12), 124501.
- 467 BERGERON, V., BONN, D., MARTIN, J. Y. & VOVELLE, L. 2000 Controlling droplet deposition
468 with polymer additives. *Nature* **405** (6788), 772–775.
- 469 BERNY, A., POPINET, S., SÉON, T. & DEIKE, L. 2021 Statistics of jet drop production. *Geophys.*
470 *Res. Lett.* **48** (10), e2021GL092919.
- 471 BERTIN, V. 2023 Similarity solutions in elastohydrodynamic bouncing. *arXiv preprint arXiv:2308.10754*.
- 472 BIANCE, A.-L., CHEVY, F., CLANET, C., LAGUBEAU, G. & QUÉRÉ, D. 2006 On the elasticity
473 of an inertial liquid shock. *J. Fluid Mech.* **554**, 47–66.
- 474 BILOTTO, J., KOLINSKI, J. M., LECAMPION, B., MOLINARI, J.-F., SUBHASH, G. & GARCIA-
475 SUAREZ, J. 2023 Fluid-mediated impact of soft solids. *arXiv preprint arXiv:2311.09953*
- 476 .
- 477 BONN, D., EGGLERS, J., INDEKEU, J., MEUNIER, J. & ROLLEY, E. 2009 Wetting and spreading.
478 *Rev. Mod. Phys.* **81** (2), 739–805.
- 479 BORMASHENKO, E., POGREB, R., WHYMAN, G. & ERLICH, M. 2007 Resonance Cassie-Wenzel
480 wetting transition for horizontally vibrated drops deposited on a rough surface. *Langmuir*
481 **23** (24), 12217–12221.
- 482 BOUROUIBA, L. 2021 The fluid dynamics of disease transmission. *Annu. Rev. Fluid Mech.* **53**,
483 473–508.
- 484 BOUWHUIS, W., VAN DER VEEN, R. C. A., TRAN, T., KEIJ, D. L., WINKELS, K. G., PETERS,
485 I. R., VAN DER MEER, D., SUN, C., SNOEIJER, J. H. & LOHSE, D. 2012 Maximal air
486 bubble entrainment at liquid-drop impact. *Phys. Rev. Lett.* **109** (26), 264501.
- 487 BRACKBILL, J. U., KOTHE, D. B. & ZEMACH, C. 1992 A continuum method for modeling
488 surface tension. *J. Comput. Phys.* **100** (2), 335–354.
- 489 CALLIES, M. & QUÉRÉ, D. 2005 On water repellency. *Soft Matter* **1** (1), 55–61.
- 490 CHANTELOT, P. 2018 Rebonds spéciaux de liquides. PhD thesis, Université Paris-Saclay
491 (ComUE).
- 492 CHEN, X., MA, R., LI, J., HAO, C., GUO, W., LUK, B. L., LI, S. C., YAO, S. & WANG, Z.
493 2012 Evaporation of droplets on superhydrophobic surfaces: surface roughness and small
494 droplet size effects. *Phys. Rev. Lett.* **109** (11), 116101.
- 495 CHENG, N.-S. 2008 Formula for the viscosity of a glycerol–water mixture. *Ind. Eng. Chem. Res.*
496 **47** (9), 3285–3288.
- 497 CHENG, X., SUN, T.-P. & GORDILLO, L. 2022 Drop impact dynamics: impact force and stress
498 distributions. *Annu. Rev. Fluid Mech.* **54**, 57–81.
- 499 CHEVY, F., CHEPELIANSKII, A., QUÉRÉ, D. & RAPHAËL, E. 2012 Liquid Hertz contact: softness
500 of weakly deformed drops on non-wetting substrates. *Europhys. Lett.* **100** (5), 54002.
- 501 CHO, H. J., PRESTON, D. J., ZHU, Y. & WANG, E. N. 2016 Nanoengineered materials for
502 liquid–vapour phase-change heat transfer. *Nat. Rev. Mater.* **2** (2), 16092.
- 503 CHUBYNSKY, M. V., BELOUSOV, K. I., LOCKERBY, D. A. & SPRITTLES, J. E. 2020 Bouncing
504 off the walls: the influence of gas-kinetic and van der Waals effects in drop impact. *Phys.*
505 *Rev. Lett.* **124**, 084501.
- 506 CLANET, C., BÉGUIN, C., RICHARD, D. & QUÉRÉ, D. 2004 Maximal deformation of an
507 impacting drop. *J. Fluid Mech.* **517**, 199–208.
- 508 DA VINCI, L. 1508 *Codex Hammer* (earlier *Codex Leicester*). In *The Notebooks of Leonardo da*
509 *Vinci* (ed. and trans. E. MacCurdy).. George Braziller.
- 510 DE GENNES, P. G. 1985 Wetting: statics and dynamics. *Rev. Mod. Phys.* **57**, 827–863.
- 511 DENG, X., MAMMEN, L., BUTT, H.-J. & VOLLMER, D. 2012 Candle soot as a template for a
512 transparent robust superamphiphobic coating. *Science* **335** (6064), 67–70.
- 513 DRISCOLL, M. M. & NAGEL, S. R. 2011 Ultrafast interference imaging of air in splashing
514 dynamics. *Phys. Rev. Lett.* **107** (15), 154502.
- 515

- 516 EGGERS, J., FONTELOS, M. A., JOSSERAND, C. & ZALESKI, S. 2010 Drop dynamics after
517 impact on a solid wall: theory and simulations. *Phys. Fluids* **22** (6), 062101.
- 518 FUKAI, J., SHIIBA, Y., YAMAMOTO, T., MIYATAKE, O., POULIKAKOS, D., MEGARIDIS, C. M.
519 & ZHAO, Z. 1995 Wetting effects on the spreading of a liquid droplet colliding with a flat
520 surface: experiment and modeling. *Phys. Fluids* **7**, 236–247.
- 521 GARCÍA-GEIJO, P., RIBOUX, G. & GORDILLO, JM 2024 The skating of drops impacting over gas
522 or vapour layers. *J. Fluid Mech.* **980**, A35.
- 523 GAUTHIER, A., SYMON, S., CLANET, C. & QUÉRÉ, D. 2015 Water impacting on
524 superhydrophobic macrotextures. *Nat. Commun.* **6** (1), 1–6.
- 525 GOHARDANI, O. 2011 Impact of erosion testing aspects on current and future flight conditions.
526 *Prog. Aerosp. Sci.* **47** (4), 280–303.
- 527 GORDILLO, J. M., RIBOUX, G. & QUINTERO, E. S. 2019 A theory on the spreading of impacting
528 droplets. *J. Fluid Mech.* **866**, 298–315.
- 529 GORDILLO, L., SUN, T.-P. & CHENG, X. 2018 Dynamics of drop impact on solid surfaces:
530 evolution of impact force and self-similar spreading. *J. Fluid Mech.* **840**, 190–214.
- 531 GORIN, B., DI MAURO, G., BONN, D. & KELLAY, H. 2022 Universal aspects of droplet spreading
532 dynamics in Newtonian and non-Newtonian fluids. *Langmuir* **38** (8), 2608–2613.
- 533 HAO, C., LIU, Y., CHEN, X., LI, J., ZHANG, M., ZHAO, Y. & WANG, Z. 2016 Bioinspired
534 interfacial materials with enhanced drop mobility: from fundamentals to multifunctional
535 applications. *Small* **12** (14), 1825–1839.
- 536 HE, L., DING, L., LI, B., MU, W., LI, P. & LIU, F. 2021 Optimization strategy to
537 inhibit droplets rebound on pathogen-modified hydrophobic surfaces. *ACS Appl. Mater.
538 Interfaces* **13** (32), 38018–38028.
- 539 HOFFMAN, H., SIJS, R., DE GOEDE, T. & BONN, D. 2021 Controlling droplet deposition with
540 surfactants. *Phys. Rev. Fluids* **6** (3), 033601.
- 541 JHA, A., CHANTELOT, P., CLANET, C. & QUÉRÉ, D. 2020 Viscous bouncing. *Soft Matter* **16**,
542 7270–7273.
- 543 JI, B., YANG, Z. & FENG, J. 2021 Compound jetting from bubble bursting at an air-oil-water
544 interface. *Nat. Commun.* **12** (1), 6305.
- 545 JIN, P., ZHAO, K., BLIN, Z., ALLAIS, M., MOUTERDE, T. & QUÉRÉ, D. 2023 When marbles
546 challenge pearls. *J. Chem. Phys.* **158** (20).
- 547 JOSSERAND, C. & THORODDSEN, S. T. 2016 Drop impact on a solid surface. *Annu. Rev. Fluid
548 Mech.* **48**, 365–391.
- 549 JOWKAR, S. & MORAD, M. R. 2019 Rebounding suppression of droplet impact on hot surfaces:
550 effect of surface temperature and concaveness. *Soft Matter* **15** (5), 1017–1026.
- 551 KIM, J. 2007 Spray cooling heat transfer: The state of the art. *Int. J. Heat Fluid Flow* **28** (4),
552 753–767.
- 553 KIM, S., WU, Z., ESMAILI, E., DOMBROSKIE, J. J & JUNG, S. 2020 How a raindrop gets
554 shattered on biological surfaces. *Proc. Natl. Acad. Sci. U.S.A.* **117** (25), 13901–13907.
- 555 KOLINSKI, J. M., MAHADEVAN, L. & RUBINSTEIN, S. M. 2014 Drops can bounce from perfectly
556 hydrophilic surfaces. *Europhys. Lett.* **108**, 24001.
- 557 KOOIJ, S., SIJS, R., DENN, M. M., VILLERMAUX, E. & BONN, D. 2018 What determines the
558 drop size in sprays? *Phys. Rev. X* **8** (3), 031019.
- 559 LAAN, N., DE BRUIN, K. G., BARTOLO, D., JOSSERAND, C. & BONN, D. 2014 Maximum
560 diameter of impacting liquid droplets. *Phys. Rev. Appl.* **2** (4), 044018.
- 561 LAFUMA, A. & QUÉRÉ, D. 2003 Superhydrophobic states. *Nat. Mater.* **2** (7), 457–460.
- 562 LANGLEY, K., LI, E. Q. & THORODDSEN, S. T. 2017 Impact of ultra-viscous drops: air-film
563 gliding and extreme wetting. *J. Fluid Mech.* **813**, 647–666.
- 564 LESSER, M. B. 1981 Analytic solution of liquid-drop impact problems. *Proc. R. Soc. Lond. A*
565 **377** (1770), 289–308.
- 566 LI, J., ZHANG, B., GUO, P. & LV, Q. 2014 Impact force of a low speed water droplet colliding
567 on a solid surface. *J. Appl. Phys.* **116** (21), 214903.
- 568 LI, Y., QUÉRÉ, D., LV, C. & ZHENG, Q. 2017 Monostable superrepellent materials. *Proc. Natl
569 Acad. Sci. USA* **114** (13), 3387–3392.
- 570 LIU, M., WANG, S. & JIANG, L. 2017 Nature-inspired superwettability systems. *Nat. Rev.
571 Mater.* **2** (7), 17036.

- 572 LOHSE, D. 2022 Fundamental fluid dynamics challenges in inkjet printing. *Annu. Rev. Fluid
573 Mech.* **54**, 349–382.
- 574 LOHSE, D. & VILLERMAUX, E. 2020 Double threshold behavior for breakup of liquid sheets.
575 *Proc. Natl. Acad. Sci. U.S.A.* **117**, 18912–18914.
- 576 MA, Y. & HUANG, H. 2023 Scaling maximum spreading of droplet impacting on flexible
577 substrates. *J. Fluid Mech.* **958**, A35.
- 578 MANDRE, S., MANI, M. & BRENNER, M. P. 2009 Precursors to splashing of liquid droplets on
579 a solid surface. *Phys. Rev. Lett.* **102** (13), 134502.
- 580 MARTOZET, G., JØRGENSEN, L., PELET, Y., BIANCE, A.-L. & BARENTIN, C. 2021 Dynamic
581 arrest during the spreading of a yield stress fluid drop. *Phys. Rev. Fluids* **6** (4), 044006.
- 582 MIRELS, H. 1955 Laminar boundary layer behind shock advancing into stationary fluid. *NACA
583 TN* **3401**, 25.
- 584 MITCHELL, B. R., KLEWICKI, J. C., KORKOLIS, Y. P. & KINSEY, B. L. 2019 The transient
585 force profile of low-speed droplet impact: measurements and model. *J. Fluid Mech.* **867**,
586 300–322.
- 587 MOLÁČEK, J. & BUSH, J. W. M. 2012 A quasi-static model of drop impact. *Phys. Fluids*
588 **24** (12), 127103.
- 589 NEARING, M. A., BRADFORD, J. M. & HOLTZ, R. D. 1986 Measurement of force vs. time
590 relations for waterdrop impact. *Soil Sci. Soc. Am. J.* **50**, 1532–1536.
- 591 PAPADOPOULOS, P., MAMMEN, L., DENG, X., VOLLMER, D. & BUTT, H.-J. 2013 How
592 superhydrophobicity breaks down. *Proc. Natl Acad. Sci. USA* **110** (9), 3254–3258.
- 593 PHILIPPI, J., LAGRÉE, P.-Y. & ANTKOWIAK, A. 2016 Drop impact on a solid surface: short-time
594 self-similarity. *J. Fluid Mech.* **795**, 96–135.
- 595 PÖHLKER, M. L., PÖHLKER, C., KRÜGER, O. O., FÖRSTER, J.-D., BERKEMEIER, T., ELBERT,
596 W., FRÖHLICH-NOWOISKY, J., PÖSCHL, U., BAGHERI, G., BODENSCHATZ, E., HUFFMAN,
597 J. A., SCHEITHAUER, S. & MIKHAILOV, E. 2023 Respiratory aerosols and droplets in the
598 transmission of infectious diseases. *Rev. Mod. Phys.* **95** (4), 045001.
- 599 POPINET, S. 2009 An accurate adaptive solver for surface-tension-driven interfacial flows. *J.
600 Comput. Phys.* **228** (16), 5838–5866.
- 601 POPINET, S. 2018 Numerical models of surface tension. *Annu. Rev. Fluid Mech.* **50**, 49–75.
- 602 POPINET, S. & COLLABORATORS 2013–2023 Basilisk C: volume of fluid method. [http://
603 basilisk.fr](http://basilisk.fr) (Last accessed: August 23, 2023).
- 604 QUÉRÉ, D. 2008 Wetting and roughness. *Annu. Rev. Mater. Res.* **38**, 71–99.
- 605 RAMÍREZ-SOTO, O., SANJAY, V., LOHSE, D., PHAM, J. T. & VOLLMER, D. 2020 Lifting a sessile
606 drop from a superamphiphobic surface with an impacting one. *Sci. Adv.* **6**, eaba4330.
- 607 REIN, M. 1993 Phenomena of liquid drop impact on solid and liquid surfaces. *Fluid Dyn. Res.*
608 **12**, 61–93.
- 609 RENARDY, Y., POPINET, S., DUCHEMIN, L., RENARDY, M., ZALESKI, S., JOSSERAND, C.,
610 DRUMRIGHT-CLARKE, M. A., RICHARD, D., CLANET, C. & QUÉRÉ, D. 2003 Pyramidal
611 and toroidal water drops after impact on a solid surface. *J. Fluid Mech.* **484**, 69–83.
- 612 RIBOUX, G. & GORDILLO, J. M. 2014 Experiments of drops impacting a smooth solid surface:
613 a model of the critical impact speed for drop splashing. *Phys. Rev. Lett.* **113** (2), 024507.
- 614 RICHARD, D., CLANET, C. & QUÉRÉ, D. 2002 Contact time of a bouncing drop. *Nature*
615 **417** (6891), 811–811.
- 616 RICHARD, D. & QUÉRÉ, D. 2000 Bouncing water drops. *Europhys. Lett.* **50** (6), 769–775.
- 617 SANJAY, V. 2022 Viscous Free-Surface Flows. PhD thesis, University of Twente.
- 618 SANJAY, V. 2023 VatsalSy/Impact-forces-of-water-drops-falling-on- superhydrophobic-
619 surfaces: Impact Forces of Water Drops Falling on Superhydrophobic Surfaces.
620 <https://doi.org/10.5281/zenodo.7598181>.
- 621 SANJAY, V., CHANTELOT, P. & LOHSE, D. 2023a When does an impacting drop stop bouncing?
622 *Journal of Fluid Mechanics* **958**, A26.
- 623 SANJAY, V., LAKSHMAN, S., CHANTELOT, P., SNOEIJER, J. H. & LOHSE, D. 2023b Drop impact
624 on viscous liquid films. *J. Fluid Mech.* **958**, A25.
- 625 SANJAY, V. & LOHSE, D. 2024 The unifying theory of scaling in drop impact: forces & maximum
626 spreading diameter. *In preparation*.
- 627 SANJAY, V., LOHSE, D. & JALAAL, M. 2021 Bursting bubble in a viscoplastic medium. *J. Fluid
628 Mech.* **922**, A2.

- SANJAY, V., SEN, U., KANT, P. & LOHSE, D. 2022 Taylor-Culick retractions and the influence of the surroundings. *J. Fluid Mech.* **948**, A14.
- SBRAGAGLIA, M., PETERS, A. M., PIRAT, C., BORKENT, B. M., LAMMERTINK, R. G. H., WESSLING, M. & LOHSE, D. 2007 Spontaneous breakdown of superhydrophobicity. *Phys. Rev. Lett.* **99** (15), 156001.
- SCHLICHTING, H. 1968 *Boundary-layer theory*. McGraw-Hill.
- SCHROLL, R. D., JOSSERAND, C., ZALESKI, S. & ZHANG, W. W. 2010 Impact of a viscous liquid drop. *Phys. Rev. Lett.* **104** (3), 034504.
- SHARMA, P. K. & DIXIT, H. N. 2021 Regimes of wettability-dependent and wettability-independent bouncing of a drop on a solid surface. *J. Fluid Mech.* **908**, A37.
- SHIRI, S. & BIRD, J. C. 2017 Heat exchange between a bouncing drop and a superhydrophobic substrate. *Proc. Natl. Acad. Sci. U.S.A.* **114** (27), 6930–6935.
- SIJS, R. & BONN, D. 2020 The effect of adjuvants on spray droplet size from hydraulic nozzles. *Pest. Manage. Sci.* **76** (10), 3487–3494.
- SMITH, F. R. & BRUTIN, D. 2018 Wetting and spreading of human blood: recent advances and applications. *Curr. Opin. Colloid Interface Sci.* **36**, 78–83.
- SMITH, F. R., NICLOUX, C. & BRUTIN, D. 2018 Influence of the impact energy on the pattern of blood drip stains. *Phys. Rev. Fluids* **3** (1), 013601.
- SMITH, M. I. & BERTOLA, V. 2010 Effect of polymer additives on the wetting of impacting droplets. *Phys. Rev. Lett.* **104**, 154502.
- SOTO, D., DE LARIVIERE, A. B., BOUTILLON, X., CLANET, C. & QUÉRÉ, D. 2014 The force of impacting rain. *Soft Matter* **10** (27), 4929–4934.
- SPRITLES, JAMES E 2024 Gas microfilms in droplet dynamics: When do drops bounce? *Annu. Rev. Fluid Mech.* **56**, 91–118.
- THORAVAL, M.-J., SCHUBERT, J., KARPITSCHKA, S., CHANANA, M., BOYER, F., SANDOVAL-NAVAL, E., DIJKSMAN, J. F., SNOEIJER, J. H. & LOHSE, D. 2021 Nanoscopic interactions of colloidal particles can suppress millimetre drop splashing. *Soft Matter* **17** (20), 5116–5121.
- THORAVAL, M.-J., TAKEHARA, K., ETOH, T. G. & THORODDSEN, S. T. 2013 Drop impact entrapment of bubble rings. *J. Fluid Mech.* **724**, 234–258.
- TSAI, P., LAMMERTINK, R. G. H., WESSLING, M. & LOHSE, D. 2010 Evaporation-triggered wetting transition for water droplets upon hydrophobic microstructures. *Phys. Rev. Lett.* **104** (11), 116102.
- TUTEJA, A., CHOI, W., MA, M., MABRY, J. M., MAZZELLA, S. A., RUTLEDGE, G. C., MCKINLEY, G. H. & COHEN, R. E. 2007 Designing superoleophobic surfaces. *Science* **318** (5856), 1618–1622.
- VILLERMAUX, E. 2020 Fragmentation versus cohesion. *J. Fluid Mech.* **898**, P1.
- VILLERMAUX, E. & BOSSA, B. 2011 Drop fragmentation on impact. *J. Fluid Mech.* **668**, 412–435.
- VILLERMAUX, E., WANG, X. & DEIKE, L. 2022 Bubbles spray aerosols: certitudes and mysteries. *Proc. Natl. Acad. Sci. Nexus* **1** (5), pgac261.
- VOLK, A. & KÄHLER, C. J. 2018 Density model for aqueous glycerol solutions. *Exp. Fluids* **59** (5), 75.
- WAGNER, H. 1932 Über Stoß- und Gleitvorgänge an der Oberfläche von Flüssigkeiten. *Z. Angew. Math. Mech.* **12** (4), 193–215.
- WILDEMAN, S., VISSER, C. W., SUN, C. & LOHSE, D. 2016 On the spreading of impacting drops. *J. Fluid Mech.* **805**, 636–655.
- WORTHINGTON, A. M. 1876a On the forms assumed by drops of liquids falling vertically on a horizontal plate. *Proc. R. Soc.* **25** (171–178), 261–272.
- WORTHINGTON, A. M. 1876b A second paper on the forms assumed by drops of liquids falling vertically on a horizontal plate. *Proc. R. Soc.* **25** (171–178), 498–503.
- WU, S., DU, Y., ALSAID, Y., WU, D., HUA, M., YAN, Y., YAO, B., MA, Y., ZHU, X. & HE, X. 2020 Superhydrophobic photothermal icephobic surfaces based on candle soot. *Proc. Natl. Acad. Sci. USA* **117** (21), 11240–11246.
- XU, L., ZHANG, W. W. & NAGEL, S. R. 2005 Drop splashing on a dry smooth surface. *Phys. Rev. Lett.* **94** (18), 184505.

- 685 YARIN, A. L. 2006 Drop impact dynamics: splashing, spreading, receding, bouncing... *Annu.*
686 *Rev. Fluid Mech.* **38**, 159–192.
- 687 YARIN, A. L., ROISMAN, I. V. & TROPEA, C. 2017 *Collision Phenomena in Liquids and Solids*.
688 Cambridge University Press.
- 689 YUN, S. 2017 Bouncing of an ellipsoidal drop on a superhydrophobic surface. *Sci. Rep.* **7** (1),
690 17699.
- 691 ZHANG, B., LI, J., GUO, P. & LV, Q. 2017 Experimental studies on the effect of reynolds and
692 weber numbers on the impact forces of low-speed droplets colliding with a solid surface.
693 *Exp. Fluids* **58** (9), 1–12.
- 694 ZHANG, B., SANJAY, V., SHI, S., ZHAO, Y., LV, C. & LOHSE, D. 2022 Impact forces of water
695 drops falling on superhydrophobic surfaces. *Phys. Rev. Lett.* **129**, 104501.
- 696 ZHANG, R., ZHANG, B., LV, Q., LI, J. & GUO, P. 2019 Effects of droplet shape on impact
697 force of low-speed droplets colliding with solid surface. *Exp. Fluids* **60** (4), 64.
- 698 ZHENG, S., DILLAVOU, S. & KOLINSKI, J. M. 2021 Air mediates the impact of a compliant
699 hemisphere on a rigid smooth surface. *Soft Matter* **17** (14), 3813–3819.